Journal of Materials Chemistry C 8.4 (2020): 1448-1458

DOI: https://doi.org/10.1039/C9TC05185F

ARTICLE

Cunning defects: Emission control by structural point defects on Cu(I)I double chain Coordination Polymers

Received 00th January 20xx,
Accepted 00th January 20xx

DOI: 10.1039/x0xx00000x

Javier Conesa-Egea,[a,b] Javier González-Platas,[c] Ulises R. Rodríguez-Mendoza,[c] José Ignacio Martínez,[d] Pilar Ocon,[e] Vanesa Fernández-Moreira,[f] Rubén D. Costa,[g] Julio Fernández-Cestay,[g] Félix Zamora[a,b,h] and Pilar Amo-Ochoa[a,h]*

ABSTRACT: The direct reaction between CuI and 3,5-dichloropyridine, in acetonitrile at room temperature, gives rise to $[Cu(Cl_2\text{-py})I]_n$ (Cl_2-py= 3,5-dichloropyridine), which consists of a Cu(I)-I double chain based coordination polymer (CP) grafted with 3,5-dichloropyridine. In this simple one-pot process, the modulation of the reaction conditions, i.e. slight variations in the CuI and Cl_2-py ratio caused by in-situ disproportion, can, however, produce significant changes in the physical properties of the materials. For instance, the reaction carried out in a 1:1 ratio under ambient conditions leads to compound **1**, while compound **1'** is obtained upon a solvothermal process of stoichiometric reaction mixture, Cl_2-py and CuI, which produces partial disproportion (< 0.5% in weight) of the initial Cu(I). Interestingly, compounds **1** and **1'** show an identical chemical composition and structure as determined by both single crystal and powder X-ray diffraction. However, they display remarkable differences in the luminescence behavior, featuring broad emission bands centered at 515 and 670 nm and associated to photoluminescence quantum yields of 12 and 5% for **1** and **1'**, respectively. Density functional theory (DFT) calculations allowed us to rationalize the nature of this rare behavior. This is attributed to structural defects related to the weaker coordination bond present in these structures that provoke the strong red-shifted emission.

Introduction

Coordination polymers (CPs) are materials formed by self-assembly of two or more building blocks, so they are part of what is currently known as modular chemistry. In principle, their structure and physico-chemical properties can be preprogrammed by suitable selection of their building blocks. Thus, several novel multifunctional and even smart materials are currently being produced following this strategy. An interesting example of this family of materials are those formed by Cu-I double chains grafted with different N-donor ligands such as pyridine, pyrazine or pyrimidine derivatives.[1-5] This CP family shows interesting electronic properties leading to materials combining emission and semiconductivity[4, 6-11] but, on the other hand, their flexible structure, *i.e.* Cu-I double chain, is fascinating because small physical or/and chemical stimulus slightly affect the Cu-I distances and angles significantly, altering their physical properties.[12-14] This is why they have been suggested as new stimuli-response materials suitable for new sensors fabrication.

However, it is well-known that the physical properties of a material are defined not only by the atomic structure, but also by defects, which can play a fundamental role. Indeed, the presence of surface defects has been described as a cause of changes in the physical properties of a single compound.[15-17] In fact, defects of various natures and length scales are key attributes of solid-state materials and strongly affect their physical and chemical properties.[17]

Following this basis, the generation of specific defects through controlled doping, using different synthetic routes with the aim to modify the optical properties of a specific compound, has already been reported.[18, 19] In most of these investigations, the dopant species represent *ca*. 1 to 20 % and provoke significant changes in the structure and morphology of the material that can be studied by using conventional characterization techniques.[20] Therefore, it seems very important to study how to control the presence of defects[21-24] in crystalline compounds to gain control over their properties and, therefore, improve their efficiency in any of their possible applications.[25-29] In fact,

[a.] *Departamento de Química Inorgánica, Universidad Autónoma de Madrid, 28049 Madrid, Spain. E-mail: pi-lar.amo@uam.es*
[b.] *Condensed Matter Physics Center (IFIMAC), Universidad Autónoma de Madrid, 28049 Madrid, Spain*
[c.] *Departamento de Física. Instituto Universitario de Estudios Avanzados en Física Atómica, Molecular y Fotónica (IUDEA). MALTA Consolider Team. Universidad de La Laguna, Avda. Astrofísico Fco. Sánchez s/n, La Laguna, Teneri-fe, E-38204, Spain.*
[d.] *Departamento de Nanoestructuras, Superficies, Recubrimientos y Astrofísica Molecular, Instituto de Ciencia de Ma-teriales de Madrid (ICMM-CSIC), 28049 Madrid, Spain*
[e.] *Departamento de Química Física, Universidad Autónoma de Madrid, 28049 Madrid, Spain*
[f.] *Departamento de Química Inorgánica, Instituto de Síntesis Química y Catálisis Homogénea (ISQCH), CSIC-Universidad de Zaragoza, 50009 Zaragoza, Spain*
[g.] *IMDEA Materials Institute, Calle Eric Kandel 2, E-28906 Getafe, Madrid, Spain.*
[h.] *Institute for Advanced Research in Chemical Sciences (IAdChem), Universidad Autónoma de Madrid, 28049 Madrid, Spain*

Electronic Supplementary Information (ESI) available: Tables of Crystallographic data, X-ray powder diffractograms, emission spectra and additional Figures. See DOI: 10.1039/x0xx00000x

CCDC 1919665-1919681, contains the supplementary crystallographic data for this paper. These data can be obtained free of charge from The Cambridge Crystallographic Data Centre *via* www.ccdc.cam.ac.uk/data_request/cif.

defect engineering is of paramount importance to manipulate crystal quality and, therefore, the specific properties desired in a material. However, the study of structural defects is very complicated in particular for low dimensionality defects present in low concentration where the usual spectroscopic and diffractometric techniques (IR, XRD, XPS…) do not give this information.[16] In case of Metal Organic Frameworks (MOFs), engineered defects have gained recent attention because their implications in both catalysis and porosity.[17] Despite this, still very little work reports the effect of the structural defects of CPs on their electronic properties. Very recently we have shown that the electrical conductivity of MMX chains, a particular type of CPs well-related to CuI-double chains, strongly varies with the density and type of the metal-halide defects along the MMX chains.[30]

Herein, we provide a rare case in which the strong influence of the structural defects caused by the simple modification of the synthetic conditions can modulate the structural defect concentration in the crystals of $[Cu(Cl_2\text{-py})I]_n$ (Cl_2-py= 3,5-dichloropyridine), affecting their optical properties. Theoretical calculations have been used to rationalize the nature and the remarkable influence of the structural point defects along the CuI double chains and the electronic properties in these materials.

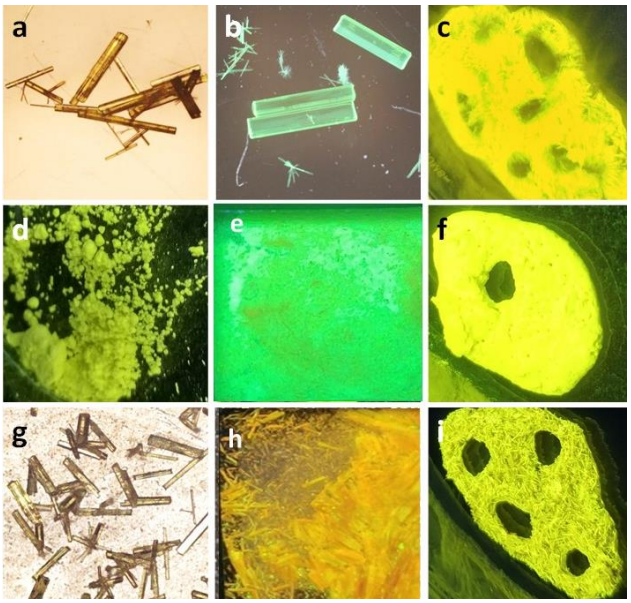

Figure 1. Images of **1** as crystals at 300 K and ambient light (a), under UV light of λ = 365 nm (b) and at 80 K under the same UV light (c). (d,e,f) images of **1** as a polycrystalline solid at 300 K and ambient light (d), under UV light of λ = 450 nm (e) and at 80 K under the same UV light (f). (g, h, i) images of **1'** at 300 K and ambient light (g), under UV light of λ = 450 nm (h) and at 80 K under the same UV light (i). The spectroscopic and analytical characterization of **1** and **1'** do not show any significant difference (Figure S1 and S2).

Results and discussion

Synthesis and Structure

The direct reaction between CuI and 3,5-dicloropyridine (Cl_2-py) in acetonitrile gives rise to the isolation of the CP $[Cu(Cl_2\text{-py})I]_n$. However, two different compounds, named as **1** and **1'**, with same structure and composition have been isolated upon slight modifications of the synthetic conditions. Thus, when the initial CuI and Cl_2-py acetronitrile solution, in a 1:1 ratio and a range of concentration (*ca*. 18-70 mM), is allowed to crystallize at 25 ^{0}C, yellow single crystals of **1** are isolated. However, when the initial acetronitrile solution, in a similar range of concentrations, is first submitted to a solvothermal treatment at 120 ^{0}C for 72 h, then filtered or centrifuged and allowed to crystallize, dark-yellow crystals of **1'** are formed instead (Scheme 1). Note that crystals of both **1** and **1'** are obtained from their respective mother solution after all solid impurities have been removed. It is worth mentioning that we have testing the reproducibility of all the reactions summarized in Scheme 1, using different commercial source of the copper(I) iodide.

Interestingly, the optical properties of **1** and **1'** evaluated by naked-eye show that at room temperature crystals of **1** display a bright greenish emission that shifts to yellow at 80 K (Figure 1a-f). While crystals of **1'** display weak orange light emission at room temperature shifting to yellow at 80 K (Figure 1g-i). These are reversible thermochromic processes, since the return to their previous emission occurs upon warming back to 300 K.

Single crystal X-ray analyses of **1** and **1'** show that these structures do not present any significant difference neither in distances nor in angles (Tables S1-S2). The structure of **1** and **1'** corresponds to the general formula $[Cu(Cl_2\text{-py})I]_n$ that consists of a polymeric staircase motif of copper-iodine which runs parallel to the *b* axis, anchored with 3,5-dichloropyridine (Figures 2, S1 and S2). CPs based on Cu_2I_2 double chains have been already reported.[31, 32] The main crystal data and structure refinement parameters conditions are collected in Table S1.

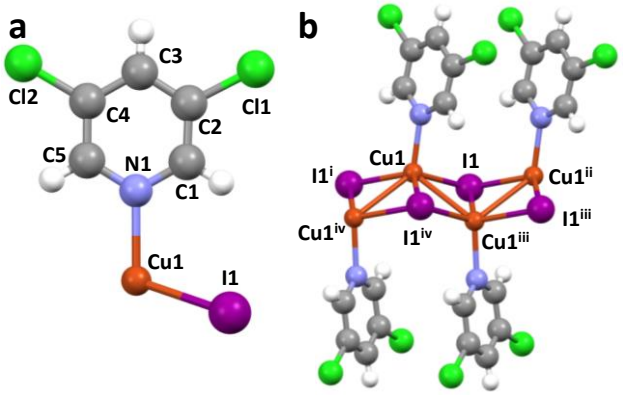

Figure 2. (a) Asymmetric unit and labelling scheme for crystals of **1** and **1'** at room conditions. (b) View of a 1D staircase chain of **1** and **1'** parallel to the *b*-axis. Symmetry codes: i=x,-1+y, z; ii=x,1+y,z; iii=1-x,1/2+y, ½-z; iv=1-x,-1/2+y,1/2-z. Legend: C, grey; H, White; N, blue; Cl, Green; Cu, orange; I, purple.

In $[Cu(Cl_2\text{-py})I]_n$ each copper(I) atom is four-coordinated, as it is bound to three iodine atoms and the iminic nitrogen of the 3,5-

dichloropyridine. The shape and geometry of this coordination environment can be described by a single geometric index[33] called τ_4 that takes a value of 1.0 for perfect tetrahedral configuration, while it will be 0.0 in the case of perfect square-planar configuration. In the case of intermediate configurations, such as trigonal pyramidal, the τ_4 parameter will have a value between 0.0 and 1.0. In the complex under study the τ_4 is 0.89, indicating a distorted trigonal pyramidal configuration. The iodine atom is three-coordinated, and the organic ligands preserve their planarity. Geometric parameters for $[Cu(Cl_2\text{-}py)I]_n$ are similar to the values measured in similar stair-cases in copper iodine structures with organic ligands contained in the CSD Database (version 5.39).[34] We have found 2.6175(6) Å for Cu-I and 2.085(4) Å for Cu-N distances, respectively. They are similar with mean values of 2.66(5) Å and 2.04(3) Å calculated in the CSD. For angles, the value for I-Cu-N in our complex is 110.35(10)° while the average value obtained from CSD was 110(5)°. In the case of I-Cu-I angles, this parameter is located in a range from 93.02° to 119.37°. In the present compound these values are 106.14(2)° and 116.97(2)°. The shorter Cu···Cu distance is 2.8113(7) Å and centroid - centroid distances between pyridine rings are equal to 4.237(3) Å.

After solvothermal reaction, we have observed in the mother liquor that faster crystallization process (25ºC), favour the presence of structural defects in the crystals, therefore giving rise to compound **1'**, whereas when the crystallization is slower, (4ºC), the less defective compound **1** is also isolated (scheme 1).

Interestingly, compound **1'** is transformed in **1** by slow recrystallization in acetonitrile at 25 ^{0}C. Additionally, when the reaction conditions were adjusted to produce an equimolecular mixture of **1** and **1'** in acetonitrile, recrystallization also led to the isolation of **1** (Scheme 1). Interestingly, crystals of Compound **1** can be redissolved in acetonitrile and recrystallizing giving rise just to isolation of **1** (scheme 1). Therefore, these set of reactions confirm that the thermodynamically stable, and less defective material, corresponds to **1**. It is worth mentioning that these reactions have been carried out several times (> 3 times) and the results are highly reproducible.

Since the only synthetic difference in the formation of **1** and **1'** is the solvothermal treatment of the initial CuI and 3,5-dicloropyridine acetonitrile solution, we have focused on the comparative analysis of two initial acetonitrile solutions: the one prepared at 25 ^{0}C and that obtained by solvothermal treatment.

The experimental difference observed upon the solvothermal treatment of the CuI and Cl_2-py acetonitrile solution is the formation of a brown colloid that is removed before crystallization, in trace amount (0.5 mg per 100 mg of CuI added as starting reagent). The TXRF analysis of the solid confirms that it consists of just copper, and therefore a partial disproportion of Cu(I) into Cu(0) and Cu(II) takes place (Figure S22

We have also discarded other potential processes that may occur and coexist during the solvothermal process such as: *i*) partial 3,5-dicloropyridine degradation, *ii*) Cu(I) reduction with iodide oxidation, leading to I_2 and Cu(0) formation; *iii*) insoluble CP formation.

Ligand degradation is discarded using NMR. The ^{1}H NMR spectrum of the acetonitrile solution obtained after solvothermal process does not show any additional peak but just those corresponding to 3,5-dicloropyridine (Figures S18-S21).

On the other hand, the UV-visible spectrum of the solution obtained after the solvothermal process matches with the one obtained just by mixing the two building blocks in acetonitrile at 25 ^{0}C (Figure S23), therefore discarding the presence of iodine in solution (which would be observed by the presence of sharp and strong absorption bands centered at 242, 291 and 360 nm). Finally, the absence of iodine and chlorine in the TXRF spectrum (Figure S22) discards the possibility of an insoluble CP or metal complex.

All things considered, we confirm that partial disproportion reaction of CuI takes place with formation of elemental copper (trace amount), therefore, the solvothermal treatment implies a slight reduction of the CuI amount, relative to the Cl_2-py, but also with the presence of trace quantities of Cu(II). Indeed, it has been previously reported that solvothermal conditions, can produce small amounts of metallic copper, which can slightly alter the reaction stoichiometry.[35]

The slight alteration in the composition of the reaction mixture, together with a faster evaporation of acetonitrile, can explain the formation of more structurally defective CuI double chains (**1'**), that can be recrystallized in acetonitrile to eliminates the defects and produce a well-ordered structure (**1**).

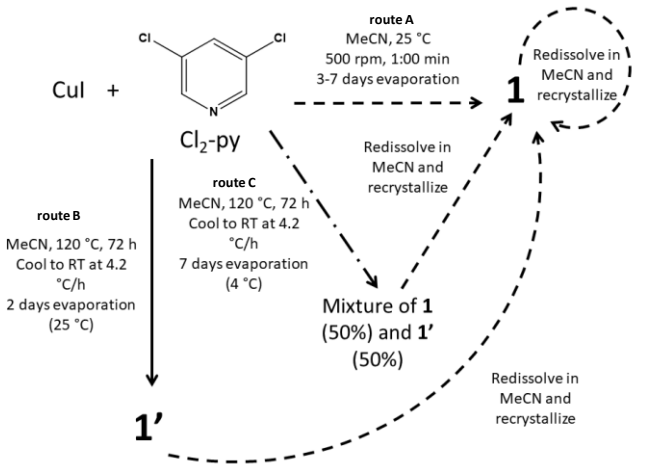

Scheme 1. Synthesis routes which lead to the formation of **1** and **1'**. The CuI-ligand stoichiometry is usually 1:1; small variations lead to the same results.

Trying to gain control over this process reactions in acetonitrile at room temperature with different CuI *vs* Cl_2-py ratios (0.95:1 and 0.9:1), were carried out. However, in all these tests formation of **1** was just observed upon crystallization. This observation suggests that the defects can only be generated under the specific experimental conditions obtained in the solvothermal process. Probably, the presence of small traces of Cu(II) and/or the presence of Cu(0) play a role in this process.

In any case, all these data confirm that the amount of defects present in **1'** is clearly below the detection limits of the

spectroscopic and diffractometric techniques (in the scale of ppm).

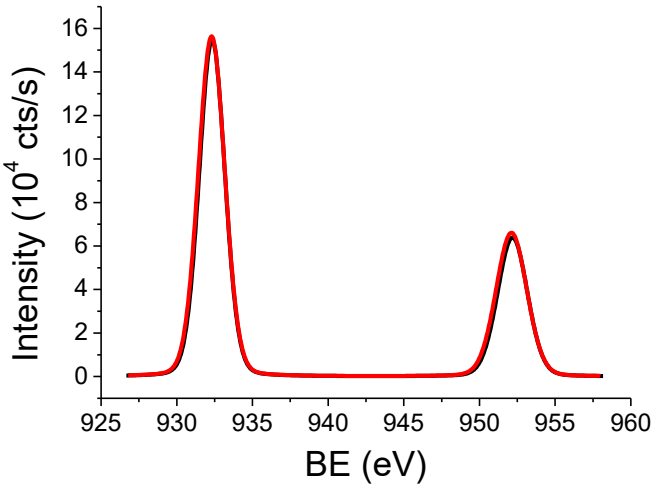

Figure 3. X-ray photoelectron spectra of **1** (black) and **1'** (red) showing the 2p energy levels of the copper centers.

Finally, XPS of **1** and **1'** were measured to corroborate whether small amounts of Cu(0) or Cu(II) could be present as defects in the crystals of **1'**, since they are not detected by other techniques. Thus, both samples show analogous peaks, corresponding to the binding energies of the electrons coming from the core orbitals of carbon, chlorine, nitrogen, iodine and copper (Table S4). As for the energy levels of copper, the emission bands relative to the 2p orbitals of copper for **1** and **1'** confirm that all the metal centers present a +I oxidation state, since the Cu(II) bands present satellite signals which cannot be observed in the XPS spectra of the CPs (Figure 3), so this tells us that the amount of copper(II) is lower than a 0.1 %, which is negligible. To confirm the presence of Cu(0) centers in **1** or **1'**, the Auger parameter of copper was studied. According to Battistoni and co-workers,[36] samples containing Cu(0) should have an Auger parameter about 2 or 3 eV lower than that of Cu(I). The results (Table S4) confirm that, since the Auger parameter does not vary from one sample to the other, all the metal centers in both samples are Cu(I). Moreover, atomic absorption spectroscopy confirms that the amount of copper in compounds **1** and **1'** is undistinguishable (Table S7).

In addition, semi-quantitative analysis carried out by Inductively Coupled Plasma Mass Spectrometry (ICP-MS) of compounds **1** and **1'** was done to determine and quantify the presence of other potential different elements present in the structures as dopants (Table S6). the ICP-MS data discard the presence of unexpected elements rather than just traces of Na and Ca but in similar quantities in **1** and **1'** (Table S6). Additionally, TXRF analysis of compounds **1** and **1'** shows traces of metals like iron or nickel in both samples, but all of them in similar ratios (Figure S24, Table S5).

These experimental data discarding the presence of dopants and strongly suggest that the cause of the different luminescence behaviour observed between **1** and **1'** is not due to dopants.

Finally, in order to check that no traces of solvents have been trapped within the structure of **1** or **1'**, a thermogravimetric analysis coupled with mass spectrometry (TG-MS) of each form of the CP was collected. It is known that Cu(I)-I CPs start decomposing at about 80 °C, losing the ligand in the first place. Thanks to the TG-MS diagrams of **1** and **1'**, we know that this loss occurs in the shape of different fragments of the pyridine ring, or as py^{2+}, but none of them correspond to acetonitrile or ethanol. On the other hand, at higher temperatures (400-800 °C), the fragment at m/z which enters the mass detector corresponds to Cu^+ or I^{2+} ions. Therefore, we can conclude that the shift in the luminescence of **1** and **1'** is not due to the presence of solvents in the structure (Figures S15 and S16).

Theoretical calculations

In order to rationalize the differences observed between **1** and **1'**, a theoretical study of the influence in their electronic structure *versus* the existence of structural defects in the Cu_2I_2 double chains from the first-principles theoretical point of view has been carried out.

Here, we have used DFT theoretical calculations to model the pristine infinite chain (SI and Figure S28) and different defective chain systems (Figure S28 a, b and c). This was realized on the basis of the structure obtained by X-ray diffraction experiments, and the relatively low bond energies of coordination bonds (15–50 kcal mol^{-1}), which lead to a certain lability and in some cases kinetic reversibility of the coordination bonds.

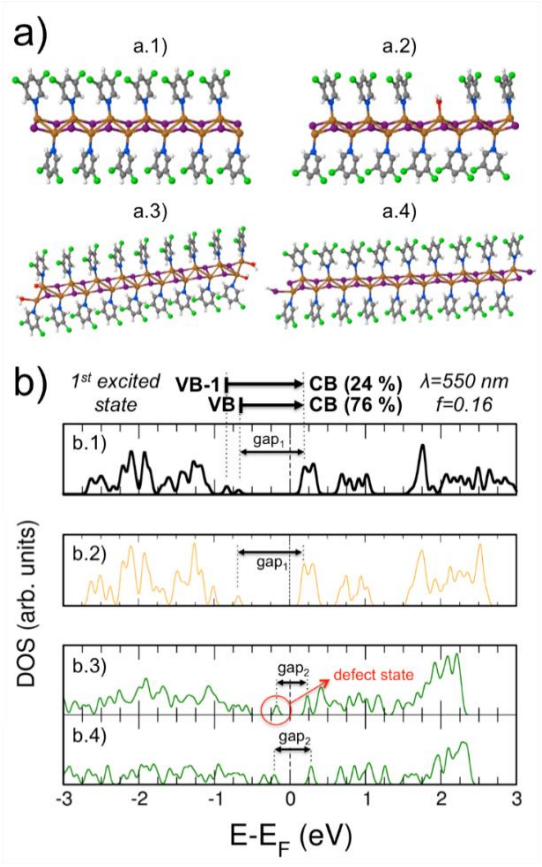

Figure 4. Computed density of states (in arb. units) as a function of the energy (referred to the Fermi energy) for: the pristine infinite chain case (a.1, b.1); an infinite defective chain with a lack of organic ligands (with a density of defects of

1/12) (a.2, b.2); 9-units defective chain fragments with two different terminating effects (a.3, a.4 and b.3 and b.4)). Electronic states involved, photon wavelength, oscillator strength and weight of the contributing transitions are shown for the most pronounced low-lying optical excitation in the infinite pristine chain. Structures are also shown for each case.

As a proof of concept, three different point defects have been considered: the two first types of defects for representative chain fragments of three different lengths: 3, 5 and 9-units chain fragments, and the third one for a defective infinite chain. The first type of defects consists in cutting a chain, leaving Cu^+ terminating atoms. Charge compensation has been realized by alternating OH^- as counteranion and H_2O groups (Figure 4, and S28a). The second type of defect considered consists of cutting an infinite chain leaving I^- terminating atoms, which, again, has been saturated to balance charge by alternating H^+ atoms (Figure 4 and S28b). Finally, the third type of defect considered modelled on an infinite chain has been the lack of an organic ligand (with a defect density of 1/12). The Cu dangling bond after removing the ligand has been fully relaxed and subsequently saturated by a water molecule yielding a bond-length of 2.36 Å (Figure 4 and S28c). Nonetheless, among the rest of defect types, the latter seems to be the most unlikely; since a CI-NEB (climbing-image nudge elastic band) transition state calculation corresponding to the detachment of an organic ligand from the chain yields an energy barrier > 2.2 eV, which turns this detachment mechanism unfeasible.

In order to check the influence of the modelled defects on the electronic properties of the compound, we have computed the density of electronic states (DOS) of the pristine infinite chain to be compared with that of the longest 9-units defective chain fragments and the defective infinite chain, normalized to the number of atoms per unit cell for a better comparison (Figure 4).

In Figure 4, the density of states shows a rich profile and yields an electronic band-gap between the valence and conduction bands (VB and CB, respectively) of around 0.9 eV (taking into account that the band gap is underestimated by 1.5 eV in the calculations, the actual value would be 2.4 eV). The pristine compound can be categorized as a narrow-gap n-type semiconductor with the Fermi energy very close to the conduction band. For the defective infinite chain with the lack of organic ligands (Figure 5a.2 and 5b.2), the density of states profile remains almost unaltered with a similar band-gap and semiconducting character than that obtained for the pristine case, which indicates that, electronically, the system would not be substantially affected by this kind of defects (at least for a defect concentration of 1/12). For the 9-units defective chain fragment with the defect (Cu^+ terminal), shown in Figure 5a.3 and 5b.3, its density of states profile has changed substantially. A direct comparison between this case and the DOS profile for the pristine infinite chain reveals the appearance of a defect state at around 0.2 eV below the Fermi energy within the mid-gap region. The new band-gap for this defective fragment is around 0.45 eV (1.95 eV after the correction). Finally, the 9-units defective chain fragment with the terminating (I^- terminal) defect shown in Figure 4 (a.4, b.4) shows a density of states profile also quite different to that of the pristine case. Again, a direct comparison between this situation and the DOS profile for the pristine infinite chain reveals a closing of the band-gap up to a value of 0.5 eV (2.0 eV after the correction), close to the obtained for the previous defective case. Thus, for these two defective cases we observe a reduction of the band-gap, although with two different origins, which will have a reflection in the optical properties of the system.

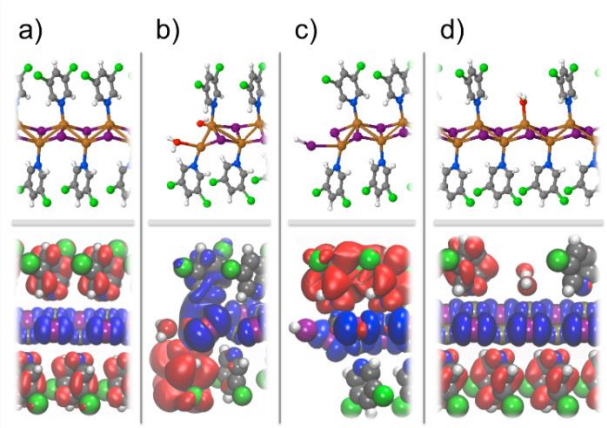

Figure 5. 3D orbital isodensities (all with a value of 10^{-3} a.u.) corresponding to the valence (blue) and conduction (red) bands for: a) the pristine infinite chain case; b) and c) defective chain fragments with two different terminating effects; and d) an infinite defective chain with a lack of organic ligands with a density of defects of 1/12.

This observation can be reinforced by computing the most pronounced low-lying optical excitation for the infinite pristine chain. This computed excitation corresponds to a combination between two electronic transitions: one from VB → CB (with a weight of around 75 %), and other from VB-1 → CB (with a weight of around 25 %) at a photon wavelength of 550 nm and with a computed oscillator strength of 0.16. Interestingly, the most important states involved in this optical transition, VB and CB, are spatially located, as usual in this kind of compounds, in the metallic skeleton and the organic ligands, respectively (Figure 5a).

At this point, it would be interesting to check the spatial distribution of the CB and VB for the three defective chain fragments analyzed (Cu^+, I^- terminal and remove the terminal ligand). Figure 5b shows that the spatial distribution of the new defect state appearing in the DOS profile of the defective chain Cu^+ fragment is also located mostly in the skeleton chain, whilst the CB is mostly located on the ligands. This could yield similar photoexcitation efficiency as happens in the pristine case but with a red-shift in the wavelength of the main peak coming from the band-gap reduction. The same effect occurs for the defective I^- chain fragment of Figure 5c; VB and CB are once again located in the metallic chain and organic ligands, respectively. Similarly, one could expect similar photoexcitation efficiency as in the previous defective case exhibiting a similar associated red-shift in the wavelength of the main peak again coming from the band-gap reduction. Nevertheless, no significant change in the photoexcitation efficiency is expected for the defective infinite chain of Figure 5d since their electronic properties rather vary w.r.t. the pristine case. Based on these

findings one could expect a red-shift in the emission properties due to the presence of the terminating Cu^{+} and I^{-} defects, whilst not for the unlikely situation of lack of organic ligands. Interestingly, the almost 2nd-order electronic degeneracy observed in the conduction band for the case of the pristine infinite chain disappears as a consequence of a visible splitting into two peaks for the cases reported in Figure 4.

This could give rise to both, new absorption bands as highlighted by the color of the crystals (Figure 1) and new photoluminescence features, that should correspond to transitions between VB-1 and VB → CB and CB+1.

Photophysical properties of 1 and 1'

Building up onto the above theoretical description, we turned to investigate the impact of the structural defects on the photoluminescence behavior under different experimental conditions. Precisely, we carried out both temperature and pressure dependence photoluminescence assays for both compounds.

First, the emission spectra (λ_{exc} = 375 nm) of **1** and **1'** was monitored at temperatures ranging from 80 to 300 K (Figure 6). Compound **1** displays, at room temperature, an asymmetric broad emission band centered at 515 nm associated to photoluminescence quantum yields of 12 % and an average excited state lifetimes (τ_{av}) of 1.9 µs. Upon decreasing the temperature, the intensity of the emission increases along with a gradually red-shift of the maximum wavelength to 530 nm with a new shoulder at *ca*. 550 nm at, for example, 80 K. Interestingly, the analysis at VT reveals that this red shift has its origin in the relative increase of a low energy structured band (530 max, 550*sh*) with respect to a second-high energy component at ~495 nm, clearly noticeable at intermediate temperatures (see 150K, for example). The noticeable increase in intensity and the vibrational spacing (~ 680 cm^{-1}) of this low energy component points out to direct band gap emission associated to CuI core – *vide supra.*

As discussed before, the general morphology of **1'** is similar to that of **1**, while the structural defects introduce intra band gap states that can be radiatively active. Following this rationale, complex **1'** shows a weak orange/yellowish emission consisting of a low energy band at ~670 nm (τ_{av} = 0.5 µs) with a broad shoulder at ~560 nm (Figure 6) that are attributed to the intra band gap emission caused by structural defects and the direct band gap emission of the core, respectively. This dual emission is noticeable weaker that the one of **1**, reaching photoluminescence quantum yields of 5%. In contrast to **1**, the decrease of the temperature leads to i) a slight blue shift of the low-energy emission band from 670 nm to ~650 nm, and ii) a significant increase in intensity of the ~560 nm shoulder, that reveals itself as a prominent structured band at 80K (530*sh*, 560_{max}, 590*sh*). This is expected since the deactivation pathway from the CB to the intra band gap defect states are hampered at low temperatures.

Joining both theoretical and photophysical evidences, Figure 6c displays the proposal for the emitting excited state scenario of **1'** ruled by the structural defects. In short, the presence of the structural defects leads to reduced photoluminescence due to the presence of a low-energy emission with a zero energy of 2.03 eV (611 nm) and a high-energy band with a zero energy of 2.21 eV (560 nm) that becomes dominant at low temperature. Interesting, the difference between the zero energy values are in line with those noted by the calculations (2.40 and 1.95 eV). In the case of **1**, as structural defect free compounds, the emission only corresponds to the direct band gap (530 nm) with zero energy of 2.34 eV. Again, the differences between the zero energy of the direct band gap of **1** and **1'** (0.13 eV) are also in good agreement with those noted by the calculations.

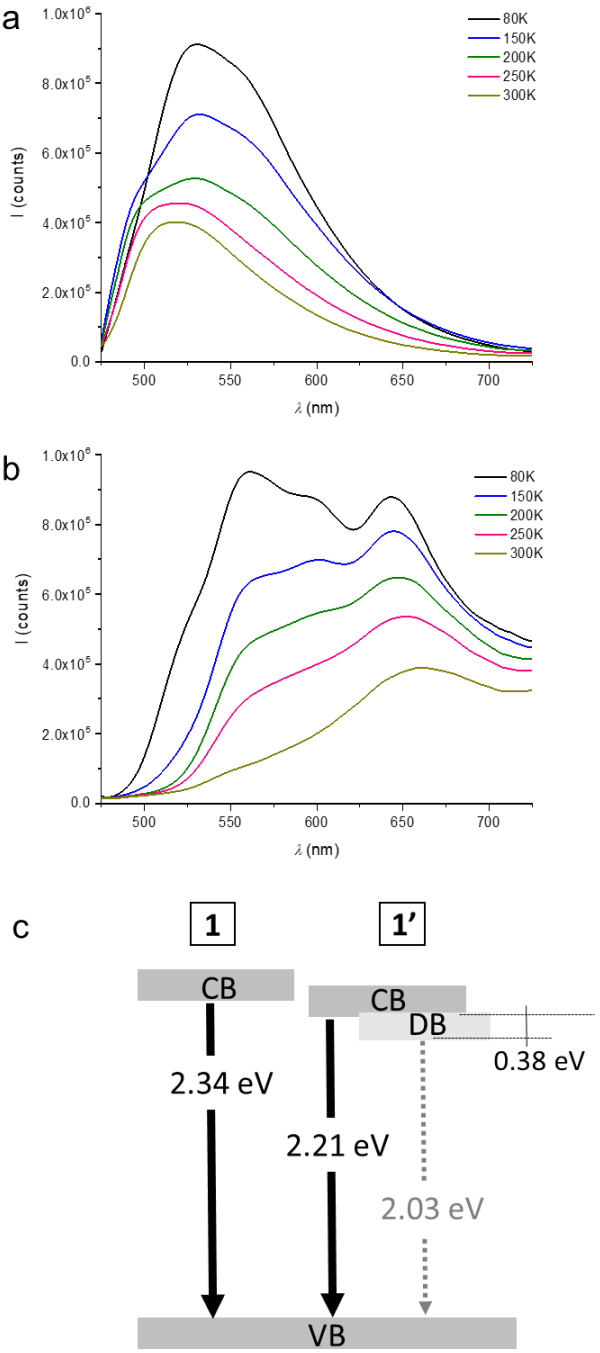

Figure 6. Thermal dependence of the emission spectra (λ_{exc} = 375 nm) of **1** (a) and **1'** (b). (c) Emitting excited state scenario of **1** and **1'** ruled by the structural defects.

Experimental

Materials and methods

All reagents and solvents purchased were used without further purification. Copper(I) iodide was purchased from Sigma-Aldrich, Riedel-De Häen and Tokyo Company International (TCI). IR spectra were recorded with a PerkinElmer 100 spectrophotometer using a universal ATR sampling accessory from 4000 to 650 cm^{-1}. Elemental analyses were performed with a LECO CHNS-932 Elemental Analyzer. Powder X-ray diffraction data was collected using a Diffractometer PANalytical X'Pert PRO with θ/2θ primary monochromator and X'Celerator fast detector. The samples have been analyzed with scanning θ/2θ. Thermogravimetric analyses (TGA) and TGA coupled with mass spectrometry (TG-MS) were carried out on a TA Instruments Q500 thermobalance oven with a Pt sample holder and mass detector; N_2 was used as purge gas, at a flow rate of 90 mL/min; the samples were heated from 25 to 1000 °C at a rate of 10 °C/min. Raman spectra were recorded in a Bruker Senterra Raman microscope, using a 785 nm laser as the excitation source, at a power of 25 mW. Inductively Coupled Plasma coupled with Mass Spectrometry (ICP-MS) was carried out in a Perkin-Elmer NexION 300XX ICP-MS Spectrometer equipped with a collision-reaction cell for interference removal. For measurements, **1** and **1'** were digested in concentrated nitric acid at 90 °C for 60 minutes, using a SCP Science Digiprep-JR open glass sample preparation system. The copper determinations *via* atomic absorption spectroscopy were carried out in an Analytic Jena ContrAA 700 high resolution continuum source atomic absorption spectrophotometer. The absorbance measurements were performed in an air-acetylene flame collecting the data at a wavelength of 324.754 nm. For the measurements, 2 mg of sample (weighed with an accuracy of 0.01 mg) were dissolved in the minimum amount of nitric acid, to reach a final concentration of 1% w/w of sample in the acid, and diluted with milli-Q water to a total volume of 100 mL. The TXRF measurements of **1**, **1'** and the residual solid obtained in the synthesis of **1'** were performed in a Bruker S2 PicoFox fixed-geometry spectrometer, using Ni/C monochromated MoK_α radiation as the energy source.

Luminescence excitation and emission spectra of the microcrystals (**1** and **1'**) of $[Cu(Cl_2\text{-py})I]_n$ (Cl_2-py= 3,5-dichloropyridine) were performed with a Jobin-Yvon Horiba Fluorolog FL-3-11 spectrometer fitted with a JYTBX picosecond detection module using band pathways between and 2 nm for both excitation and emission and also with an Edinburgh FS5 spectrofluorimeter with Xe lamp as excitation source. Measurements at variable temperature were done using an Oxford Cryostat Optistat DN with an accessory for solid samples. Lifetime measurements were recorded with a Fluoromax phosphorimeter accessory containing a UV xenon flash tube and also with a Nano a picosecond pulsed light source (450 nm). Lifetime data were fitted by using the Jobin-Yvon software package and the Origin Pro 8 program. Quantum yield determination was done with the SC-30 Integrating Sphere upgrade from the same brand. All the measurements in the solid state were made by encapsulating the corresponding solid sample between quartz plates.

The mechanical dependence of the luminescence spectra of $[Cu(Cl_2\text{-py})I]_n$ (Cl_2-py= 3,5-dichloropyridine) **1** and **1'**, were recorded exciting with a 375 nm diode laser, using a 0.75 m single grating monochromator (Spex 750M) equipped with a cooled photomultiplier tube (Hamamatsu 928b). All spectra have been corrected for the instrument response. High pressure was generated with a miniature diamond anvil cell (mini-DAC), designed at The University of Paderborn (Germany), with low luminescent II-a type diamonds for optical, infrared and diffraction measurements. A stainless-steel gasket was pre-indented to 80 µm and a centred hole of typical diameter of 150 µm constitutes the sample chamber. Ruby chips were used as pressure calibrant using the ruby R_1line fluorescence and 16:3:1 methanol-ethanol-water mixture as pressure medium that provided hydrostatic pressures up to 14 GPa.

Scanning Electron Microscopy (SEM) images were taken in a Philips XL 30 S-FEG electron microscope, applying an electron beam of 300 µA intensity and 10.0 kV potential, at a pressure of 10^{-7} Pa. In order to obtain reproducible results, very flat substrates were used with precisely controlled chemical functionalities, freshly prepared just before the chemical deposition of the samples. Doped SiO_2 surfaces were sonicated for 15 min in acetone and 15 min in 2-propanol and then dried under an Argon flow. After sample preparation, the surfaces were metallized with a 10 nm thick Cr layer, at a pressure of 10^{-3} Pa.

The X-ray photoelectron spectra (XPS) of **1** and **1'** were obtained with a VG Escalab 200R spectrometer equipped with a hemispherical electron analyzer and a $Mg_{K\alpha}$ (hν = 1254.6 eV, λ = 9.719 Å) X-ray source, powered at 120W. The contamination C_s line was selected as the kinetic energies reference, at a value of 284.6 eV. Wagner sensibility factors were used in order to quantify the different elements on the surface. Peaks were considered to be combinations of Gaussian and Lorentzian functions in an 80/20 ratio, working with a Shirley type baseline background subtraction by using XPS Peak Fit software. An estimated error of ±0.1 eV can be assumed for all measurements.

Electronic Impedance Spectroscopy (EIS) data at 298 K were collected using an Autolab electrochemical system II PGSTAT30 (Ecochemie, The Netherlands) impedance analyzer, from 1 Hz to 1 MHz with an applied voltage of 0.01 V using a two-probe method. AC measurements were performed to determine the conductivity parameters at different exposition times to acetic acid (Acetic acid) vapour (0, 1, 2, 3, 6, 12, 18 and 24 h). Through plane conductivity was determined in all samples. The 1 and 1' materials (ca. 5 mg) were pressed up to ca. 5 GPa to form pellets with an approx. area of 0.071 cm^2 and a thickness around 0.30 mm. Symmetrical stainless steel electrodes were used as electrical contact. This was made by applying a pressure of 350 N cm torque in a conductivity cell configuration SS/ [1 or 1'] /SS, where SS refers to stainless steel. Each impedance measurement was repeated three times with different pellets to corroborate the consistency of the conductivity

measurements. The subsequent Nyquist plots were obtained from the average of these three measurements (see supporting information, section S9 and figures S24 and S25).

Crystallography

Single crystal X-Ray diffraction measurements. X-ray diffraction (XRD) measurements at ambient pressure (296K and 110K) were conducted using a Bruker Kappa Apex II diffractometer with graphite-monochromated Mo Kα radiation (λ = 0.71073 Å). The measurements were processed with the CrysAlisPro software.[37] The structures of the crystals **1** and **1'** at RT and 110 K were determined by a dual-space algorithm using the SHELXT program[38] and refinement was performed using SHELXL program[39] against F^2 by full-matrix least-squares refinement. The cell parameters were determined and refined by a least-squares fit of all reflections. A semi-empirical absorption correction (SADABS) was applied. The structures were also solved by direct methods using the SIR92 program[40] and refined by full-matrix least-squares on F^2 including all reflections (SHELXL97).[41] All non-hydrogen atoms were refined anisotropically and hydrogen atoms were included in the model at calculated positions, and refined with a rigid model with their U_{iso} value to $1.2U_{eq}$ of their parent atoms. The PLATON program[42] has been used for geometric calculations. The calculations were also performed using the WINGX crystallographic software package.[43]

For XRD high-pressure measurements of **1** and **1'**, we have used a Bragg-Mini diamond anvil cell (DAC) from Almax-EasyLab, with an opening angle of 85° and anvil culets of 500µm diameter, fitted with a stainless gasket containing a hole of 200 µm diameter and 75µm depth. A methanol-ethanol-water mixture (16:3:1) was used as pressure-transmitting medium, which remains hydrostatic in the range of pressure used in our experiments[44, 45] in order to minimize deviatory stresses which can cause incorrect values for bulk modulus.[46] The sample was placed on one of the diamond anvils (diffraction side) together with a small ruby sphere as pressure sensor. The measurements were carried out in a Rigaku SuperNOVA diffractometer equipped with an EOS2 detector (CCD) and Mo radiation micro-source, and processed in the ABSORB program contained in the CrysAlisPro software considering a Gaussian type absorption. The structure was refined, for each pressure, using previous results as starting point, on F^2 by full-matrix least-squares refinement using the SHELX[38] program. Due to limitations of the opening angle of our DAC it is only possible to collect about 35-40% of the total reflections present in a full dataset at ambient conditions. In this situation, structure refinements were performed with isotropic displacement parameters for all atoms except for the heavy atoms (Cu and I) that were refined with anisotropic displacement parameters. Hydrogen atoms were included in the final procedure in the same way as for ambient conditions. Planarity restraints on the pyridine ring were used during this process.

Crystallographic data for the structures reported in this contribution have been deposited with the Cambridge Crystallographic Data Centre as supplementary publication CCDC 1919665-1919681. Copies of the data can be obtained free of charge on application to the CCDC, Cambridge, U.K. (http://www.ccdc.cam.ac.uk/).

Theoretical methods

For all the *ab-initio* structural optimizations, transition-state barriers, electronic structure properties and photoexcitation spectra simulations of the different structures, Density Functional Theory (DFT) has been used within the plane-wave scheme implemented in the QUANTUM ESPRESSO simulation package.[47] A perturbative van der Waals (vdW) correction was used to add dispersive forces to conventional DFT functionals.[48] One-electron wave-functions were expanded in a basis of plane-waves, with energy cut-offs of 450 and 550 eV for the kinetic energy and for the electronic density, respectively, which have been adjusted to achieve sufficient accuracy in the total energy. The exchange-correlation (XC) effects have been accounted by using the generalized-gradient PBE parametrization[49] and ultra-soft pseudopotentials[50] have been adopted to model the ion-electron interaction in the H, C, N, O, Cl, Cu and I atoms. In the calculations, Brillouin zones (BZ) were sampled by means of optimal Monkhorst-Pack grids, guaranteeing a full convergence in energy and electronic density. Transition states (TSs) have been investigated within the climbing-image nudge elastic band (CI-NEB) approach[51] implemented in the QUANTUM ESPRESSO package,[47] where the initial, the final, and a sufficient amount of intermediate image-states were free to fully relax. Finally, to compute individual optical transitions for the pristine infinite chain case we have used the configuration interaction single-excitation (CIS) formalism[52] as implemented in Gaussian09.[53] This implementation is computationally very demanding, but provides excellent results in both closed-shell and open-shell systems.

Synthetic procedures

Synthesis of $[Cu(Cl_2\text{-py})I]_n$ (1 and 1') microcrystals.

route a) 100 mg (0.53 mmol) of copper(I) iodide are dissolved in 10 mL of acetonitrile. On the other hand, 81 mg (0.52 mmol) of 3,5-dichloropyridine are dissolved in 5 mL of acetonitrile. Both solutions are mixed under magnetic stirring (500 rpm), giving rise to a greenish yellow solution of **1** after 1 min. The solution is filtered to eliminate impurities and left to stand at room temperature. Yellow rod crystals of **1** were obtained after 3 days of slow evaporation of this mother solution. The crystals were filtered off, washed with acetonitrile (2 x 2 mL) and ethanol (2 x 3 mL), and dried in vacuum. Yield: 122 mg (66% based on Cu). Elemental analysis calcd (%) for $C_5H_3CuICl_2N$: C 17.74, H 0.89, N 4.14; found: C 18.04, H 1.02, N 4.10; IR selected data (ATR): ṽ (cm-1) = 3123 (vw), 3063 (vw), 3044 (w), 1867 (w), 1837 (w), 1810 (w), 1781 (w), 1561 (ms), 1551 (ms), 1415 (vs), 1387 (s), 1290 (m), 1217 (m), 1109 (s), 1094 (s), 1036 (m), 1015 (m), 903 (w), 873 (vs), 848 (m), 818 (vs), 678 (vs). TG-MS: 80-200 °C: m/z = 38, 48, 50, 63, 64, 78; 600-800 °C: m/z = 63.

When the synthesis is performed doubling the concentration of the reactants, compound **1** is immediately obtained in the reaction medium as a polycrystalline solid. The characterization

data confirmed that both the solid and crystals correspond to $[Cu(Cl_2\text{-py})I]_n$ (**1**). The powder X-ray diffraction (PXRD) data confirmed the purity of both crystals and solid (Figure S3).

Route b) 100 mg (0.53 mmol) of copper(I) iodide and 80 mg (0.53 mmol) of 3,5-dichloropyridine are dissolved in 15 mL of acetonitrile. The solution is sealed in a glass vial with a Teflon cap, heated at 120 °C for 72 hours and cooled to 20 °C at a speed of 4.2 °C/h. The resulting yellow solution is filtered to eliminate impurities and left to slowly evaporate at 25 °C. After 2 days, yellow rod-like crystals (**1'**) form. The crystals are filtered off, washed with acetonitrile (2 x 2 mL) and ethanol (2 x 3 mL), and dried in vacuum. Yield: 106 mg (60% based on Cu). Elemental analysis calcd (%) for $C_5H_3CuICl_2N$: C 17.74, H 0.89, N 4.14; found: C 18.38, H 1.04, N 4.34; IR selected data (ATR): $\tilde{\nu}$ (cm-1) = 3063 (vw), 3044 (w), 1867 (w), 1837 (w), 1810 (w), 1782 (w), 1560 (ms), 1551 (ms), 1415 (vs), 1387 (s), 1290 (m), 1217 (m), 1110 (s), 1094 (s), 1037 (m), 1015 (m), 903 (w), 874 (vs), 846 (m), 817 (vs), 678 (vs). TG-MS: 80-200 °C: m/z = 38, 48, 50, 63, 64, 78; 600-800 °C: m/z = 63.

The PXRD data confirmed the purity of **1'** and the similarity of its structure to that of **1** (Figure S3).

Thermal stability studies by thermogravimetric analysis (TGA) and TG-MS confirm that both crystals (**1** and **1'**) exhibit the same behaviour (Figures S13-S16).

Route c) 100 mg (0.53 mmol) of copper(I) iodide and 80 mg (0.53 mmol) of 3,5-dichloropyridine are dissolved in 15 mL of acetonitrile. The solution is sealed in a glass vial with a Teflon cap, heated at 120 °C for 72 hours and cooled to 20 °C at a speed of 4.2 °C/h. The resulting yellow solution is filtered to eliminate impurities and left to slowly evaporate at 4 °C. After 7 days, yellow rod-like crystals (a 1:1 mixture of **1** and **1'** crystals) form. The crystals are filtered off, washed with acetonitrile (2 x 2 mL) and ethanol (2 x 3 mL), and dried in vacuum. Yield: 106 mg (60% based on Cu).

Preparation of SEM samples. 1 (solid): A sample consisting of 5 mg of **1** as a polycrystalline solid is redispersed in double-distilled water (1 mL) and a 15 µL drop is cast on a doped SiO_2 surfaced. The solid is left to adsorb for 3 minutes and the surface is cleaned with an Argon flow.

1 and **1'** (crystals): 5 mg of crystals of **1** or **1'** are dispersed in 1 mL of isopropanol; a 15 µL drop is cast on a doped SiO_2 surfaced. The solid is left to adsorb for 3 minutes and the surface is cleaned with an Argon flow. See supporting information, section S6 and figure S25.

Conclusions

The slight modulation of the synthetic conditions in the direct reaction carried out between CuI and 3,5-dichloropyridine in acetonitrile produces two coordination polymers sharing the formula $[Cu(Cl_2\text{-py})I]_n$ (Cl_2-py= 3,5-dichloropyridine), named as **1** and **1'**. These compounds present an identical structure, determined by X-ray diffraction, consisting of a Cu_2I_2 double chain based coordination polymer (CP) grafted with 3,5-dichloropyridine terminal ligands.

Even though analytical and spectroscopic techniques show that **1** and **1'** seem identical, their electronic properties, i.e. optical properties, show significant differences. Indeed, we have shown that **1** and **1'** display emission bands at room temperature centred at 515 and 670 nm associated to photoluminescence quantum yields of 12 and 5%**,** respectively. Interestingly, both the analysis of the initial reaction conditions as well as the studies carried out in the transformation reactions between **1** and **1'** confirm that the difference between **1** and **1'** can be ascribed to the presence of variable content of structural defects. Consequently, reactions carried out under thermodynamic control, long reaction times, give rise to a less defective material named as **1**, while fast precipitation or slight modification of the initial CuI vs Cl_2-py ration, yields to **1'** that should enhance the structural defects along the Cu_2I_2 double chain.

The use of theoretical calculations has allowed rationalising the effect of structural defects on the electronic properties of **1** and **1'**. In short, calculations predict that the inclusion of punctual structural defects along the Cu_2I_2 double chain (in a 10 % content, *i.e.* Cu_2I_2 double chain breakage and presence of terminal iodine or OH substitution) produce that the appearance of a defect state at around 0.2 eV below the Fermi energy within the mid-gap region and a band-gap reduction from 0.9, for the pristine structure, to *ca*. 0.45-0.5 eV for the defective ones. Additionally, the most important states involved in this optical transition, VB and CB, are spatially located in the metallic skeleton and the organic ligands and their spatial distribution for the defective chains show that VB and CB are located in the metallic chain and organic ligands, respectively. Then, a photoexcitation efficiency associated with a red-shift in the wavelength of the main peak again coming from intra band gap states is predicted, corroborating the nature of the low-energy emission observed in **1'**. This has been further assessed by temperature and pressure dependent photoluminescence assays in which direct and intra band gap emission show distinct behaviours.

Conflicts of interest

There are no conflicts to declare.

Acknowledgements

The authors thank financial support from the Spanish Ministerio de Economía y Competitividad (MAT2016-77608-C3-1-P, MAT2016-75883-C2-2-P, MAT2010-20843-C02-01, MAT2016-75586-C4-4-P, CTQ2016-75816-C2-1P, MAT2016-75586-C4-4-P) and by EU-FEDER funds. JGP thanks to Servicios Generales de Apoyo a la Investigación (SEGAI) at La Laguna University. J.I.M. acknowledges the financial support by the "Ramón y Cajal" Program of MINECO (Grant RYC-2015- 17730) and the EU via the ERC-Synergy Program (Grant ERC- 2013-SYG-610256

NANOCOSMOS). J. C. E. acknowledges the financial support by the "FPI-MINECO" Program of MINECO (Grant BES-2015-071534). R.D.C. acknowledges the program "Ayudas para la atracción de talento investigador—Modalidad 1 of the Consejería de Educación, Juventud y Deporte—Comunidad de Madrid with the Reference No. 2016-T1/IND- 1463.", Spanish MINECO for the Ramón y Cajal program (RYC-2016-20891), the Europa Excelencia program (ERC2019- 092825), and HYNANOSC (RTI2018-099504-A-C22). R.D.C. also acknowledges the 2018 Leonardo Grant for Researchers and Cultural Creators from BBVA Foundation and the FOTOART-CM project funded by Madrid region under programm P2018/NMT-4367. J. F.-C. acknowledges the Marie Skłodowska-Curie Individual Fellowships (H2020-MSCA-IF-2017). This paper is dedicated to Dmitri Mendeléyev in honour of the 150th anniversary of the discovery of the periodic table.

Notes and references

1. C. Tard, S. Perruchas, S. Maron, X. F. Le Goff, F. Guillen, A. Garcia, J. Vigneron, A. Etcheberry, T. Gacoin and J.-P. Boilot, *Chem. Mater.*, 2008, **20**, 7010-7016.
2. S. Perruchas, C. Tard, X. F. Le Goff, A. Fargues, A. Garcia, S. Kahlal, J.-Y. Saillard, T. Gacoin and J.-P. Boilot, *Inorg. Chem.*, 2011, **50**, 10682-10692.
3. I. Jeß, P. Taborsky, J. Pospíšil and C. Näther, *Dalton Trans.*, 2007, 2263-2270.
4. D. Braga, F. Grepioni, L. Maini, P. P. Mazzeo and B. Ventura, *New J. Chem.*, 2011, **35**, 339-344.
5. J. Conesa-Egea, N. Nogal, J. I. Martinez, V. Fernandez-Moreira, U. R. Rodriguez-Mendoza, J. Gonzalez-Platas, C. J. Gomez-Garcia, S. Delgado, F. Zamora and P. Amo-Ochoa, *Chem. Sci.*, 2018, **9**, 8000-8010.
6. E. Cariati and J. Bourassa, *Chem. Commun.*, 1998, 1623-1624.
7. L. r. Meng, R. Mo, H. Zhou, G. Wang, W. Chen, D. Wang and Q. Peng, *Cryst. Growth Des.*, 2010, **10**, 3387-3390.
8. X.-C. Shan, F.-L. Jiang, L. Chen, M.-Y. Wu, J. Pan, X.-Y. Wan and M.-C. Hong, *J. Mater. Chem. C*, 2013, **1**, 4339-4349.
9. P. Amo-Ochoa, K. Hassanein, C. J. Gomez-Garcia, S. Benmansour, J. Perles, O. Castillo, J. I. Martinez, P. Ocon and F. Zamora, *Chem. Commun.*, 2015, **51**, 14306-14309.
10. K. Hassanein, P. Amo-Ochoa, C. J. Gomez-Garcia, S. Delgado, O. Castillo, P. Ocon, J. I. Martinez, J. Perles and F. Zamora, *Inorg. Chem.*, 2015, **54**, 10738-10747.
11. T. H. Kim, Y. W. Shin, J. S. Kim, S. S. Lee and J. Kim, *Inorg. Chem. Commun.*, 2007, **10**, 717-719.
12. D. Tran, J. L. Bourassa and P. C. Ford, *Inorg. Chem.*, 1997, **36**, 439-442.
13. Q. Benito, B. Baptiste, A. Polian, L. Delbes, L. Martinelli, T. Gacoin, J.-P. Boilot and S. Perruchas, *Inorg. Chem.*, 2015, **54**, 9821-9825.
14. L. Maini, P. P. Mazzeo, F. Farinella, V. Fattori and D. Braga, *Faraday Disc.*, 2014, **170**, 93-107.
15. Z. Assefa, M. A. Omary, B. G. McBurnett, A. A. Mohamed, H. H. Patterson, R. J. Staples and J. P. Fackler, *Inorg. Chem.*, 2002, **41**, 6274-6280.
16. Y. Qi, H. Xu, X. Li, B. Tu, Q. Pang, X. Lin, E. Ning and Q. Li, *Chem. Mater.*, 2018, **30**, 5478-5484.
17. Z. Fang, B. Bueken, D. E. De Vos and R. A. Fischer, *Angew. Chem. Int. Ed.*, 2015, **54**, 7234-7254.
18. W. Y. Hernandez, M. A. Centeno, F. Romero-Sarria and J. A. Odriozola, *J. Phys. Chem. C*, 2009, **113**, 5629-5635.
19. A. G. Bispo, Jr., D. A. Ceccato, S. A. M. Lima and A. M. Pires, *RSC Advances*, 2017, **7**, 53752-53762.
20. G. Byzynski, C. Ribeiro and E. Longo, *Int. J. Photoen.*, 2015, 1-13.
21. T.-S. Ahn, A. M. Müller, R. O. Al-Kaysi, F. C. Spano, J. E. Norton, D. Beljonne, J.-L. Brédas and C. J. Bardeen, *J. Chem. Phys.*, 2008, **128**, 054505.
22. Y. Wang and Y. Ma, *J. Chem. Phys.*, 2014, **140**, 040901.
23. R. E. McAnally, J. A. Bender, L. Estergreen, R. Haiges, S. E. Bradforth, J. M. Dawlaty, S. T. Roberts and A. S. Rury, *J. Phys. Chem. Lett.*, 2017, **8**, 5993-6001.
24. M. A. Fusella, F. Schreiber, K. Abbasi, J. J. Kim, A. L. Briseno and B. P. Rand, *Nano Lett.*, 2017, **17**, 3040-3046.
25. W. Wang, L. Wang and Q. Zhou, *J. Solid State Chem.*, 2012, **188**, 72-76.
26. S. S. Kanmani and K. Ramachandran, *J. Mater. Sci.*, 2013, **48**, 2076-2091.
27. X. Xia, S. Xie, M. Liu, H.-C. Peng, N. Lu, J. Wang, M. J. Kim and Y. Xia, *Proceedings of the National Academy of Sciences of the United States of America*, 2013, **110**, 6669-6673.
28. S. Kiprotich, M. O. Onani and F. B. Dejene, *J. Mater. Sci.: Mater. Electron.*, 2018, **29**, 6004-6011.
29. S. Ray, G. B. Nair, P. Tadge, N. Malvia, V. Rajput, V. Chopra and S. J. Dhoble, *J. Lumin.*, 2018, **194**, 64-71.
30. P. Ares, P. Amo-Ochoa, J. M. Soler, J. Jose Palacios, J. Gomez-Herrero and F. Zamora, *Adv. Mater*, 2018, **30**, 1705645.
31. J.-C. Li, H.-X. Li, H.-Y. Li, W.-J. Gong and J.-P. Lang, *Cryst. Growth Des.*, 2016, **16**, 1617-1625.
32. Y. Song, R. Q. Fan, P. Wang, X. M. Wang, S. Gao, X. Du, Y. L. Yang and T. Z. Luan, *J. Mater. Chem. C*, 2015, **3**, 6249-6259.
33. L. Yang, D. R. Powell and R. P. Houser, *Dalton Trans.*, 2007, 955-964.
34. F. H. Allen, *Acta Cryst. B*, 2002, **58**, 380-388.
35. Y. Li, Q. Wang, P. Liu, X. Yang, G. Du and Y. Liu, *Ceram. Int.*, 2015, **41**, 4248-4253.
36. C. Battistoni, G. Mattogno, E. Paparazzo and L. Naldini, *Inorg. Chim. Acta*, 1985, **102**, 1-3.
37. CrysAlisPro Software system, *Rigaku Corporation, Oxford, UK*, 2017.
38. G. M. Sheldrick, *Acta Cryst.*, 2015, **A71**, 3-8.
39. G. M. Sheldrick, *Acta Cryst.*, 2008, **A64**, 112-122.
40. A. C. Altomare, M.; Giacovazzo, C.; Guagliardi, A., *J. Appl. Crystallogr.*, 1993, **26**, 343-350.
41. G. M. Sheldrick, SHELXL-97, Program for Crystal Structure Refinement; University Gottingen, Gottingen (Germany), 1997.
42. A. L. Spek, *Acta Cryst.*, 2009, **D65**, 148-155.
43. M. J. Prakash and M. S. Lah, *Chem. Commun.*, 2009, 3326-3341.
44. R. J. B. Angel, M.; Zhao, J.; Gatta, G.D.; Jacobsen, S. D. J., *Appl. Crystallogr.*, 2007, **40**, 26-32.
45. S. Klotz, J. C. Chervin, P. Munsch and G. L. Marchand, *J. Phys. D Appl. Phys.*, 2009, **42**, 075413.
46. D. Errandonea, A. Muñoz and J. Gonzalez-Platas, *J. Appl. Phys.*, 2014, **115**, 216101.
47. G. Paolo, B. Stefano, B. Nicola, C. Matteo, C. Roberto, C. Carlo, C. Davide, L. C. Guido, C. Matteo, D. Ismaila, C. Andrea Dal, G. Stefano de, F. Stefano, F. Guido, G. Ralph, G. Uwe, G. Christos, K. Anton, L. Michele, M.-S. Layla, M. Nicola, M. Francesco, M. Riccardo, P. Stefano, P. Alfredo, P. Lorenzo, S. Carlo, S. Sandro,

S. Gabriele, P. S. Ari, S. Alexander, U. Paolo and M. W. Renata, *J. Phys. Cond. Matter*, 2009, **21**, 395502.
48. S. Grimme, *J. Comp. Chem.*, 2006, **27**, 1787-1799.
49. J. P. Perdew, K. Burke and M. Ernzerhof, *Phys. Rev. Lett.*, 1996, **77**, 3865-3868.
50. D. Vanderbilt, *Phys. Rev. B*, 1990, **41**, 7892-7895.
51. G. Henkelman and H. Jónsson, *J. Chem. Phys.*, 2000, **113**, 9978-9985.
52. J. B. Foresman, M. Head-Gordon, J. A. Pople and M. J. Frisch, *J. Phys. Chem.*, 1992, **96**, 135-149.
53. M. J. Frisch, Gaussian 09, Revision E.01, Gaussian, Inc., Wallingford, CT, 2009.